

The liquid-to-solid transition of FUS is promoted by the condensate surface

Yi Shen^{1,2,3*}, Anqi Chen⁴, Wenyun Wang⁴, Yinan Shen⁵, Francesco Simone Ruggeri^{1,6,7}, Stefano Aime⁸, Zizhao Wang⁴, Seema Qamar⁹, Jorge R. Espinosa¹⁰, Adiran Garaizar¹⁰, Peter St George-Hyslop^{9,11,12}, Rosana Collepardo-Guevara^{1,10,13}, David A. Weitz^{4,5,14}, Daniele Vigolo^{3,15*}, Tuomas P. J. Knowles^{1,10*}

1. Yusuf Hamied Department of Chemistry, University of Cambridge, CB2 1EW Cambridge, UK
2. School of Chemical and Biomolecular Engineering, The University of Sydney, NSW 2006, Australia
3. The University of Sydney Nano Institute, The University of Sydney, NSW 2006, Australia
4. John A. Paulson School of Engineering and Applied Sciences, Harvard University, Cambridge, MA 02138, USA
5. Department of Physics, Harvard University, Cambridge, MA 02138, USA.
6. Laboratory of Organic Chemistry, Wageningen University, 6708 WE, the Netherlands
7. Physical Chemistry and Soft Matter, Wageningen University, 6708 WE, the Netherlands
8. Molecular, Macromolecular Chemistry, and Materials, ESPCI Paris, CNRS, PSL University, 75005 Paris, France
9. Cambridge Institute for Medical Research, Department of Clinical Neurosciences, School of Clinical Medicine, University of Cambridge, CB2 0XY Cambridge, UK
10. Cavendish Laboratory, University of Cambridge, CB3 0HE Cambridge, UK
11. Department of Medicine (Neurology), Temerty Faculty of Medicine, University of Toronto, and University Health Network, Toronto, ON M5T 0S8, Canada.
12. Taub Institute For Research on Alzheimer's Disease and the Aging Brain, Department of Neurology, Columbia University Irvine Medical Center, New York, NY, USA 10032.
13. Department of Genetics, University of Cambridge, Cambridge, CB2 3EH Cambridge, UK
14. Wyss Institute for Biologically Inspired Engineering, Harvard University, Boston, MA 02115, USA.
15. School of Biomedical Engineering, The University of Sydney, NSW 2006, Australia

Contact: yi.shen@sydney.edu.au, daniele.vigolo@sydney.edu.au, tpjk2@cam.ac.uk

Materials and Methods

FUS condensates sample preparation

FUS protein used in this study was GFP (Green Fluorescent Protein) labelled. The purification method has been described in previous studies¹⁻³. The final purified protein was stored in the buffer with 50 mM Tris, 1 M KCl, 1 mM DTT, 5% glycerol, pH 7.4 at concentration 25 – 35 μ M. The purity of the protein was greater than 95%.

FUS protein stock was mixed with MiliQ water in a volume ratio of 1:19 to induce the LLPS. The final FUS and KCl concentrations were 1.75 – 1.25 μ M and 50 mM, respectively. FUS condensates were then incubated at room temperature for 30 min, 90 min, 5 h, 24 h for aging.

Confocal Imaging

Confocal microscope TCS SP8, Leica Microsystems with a 488-nm laser Argon and x60 oil-immersion objective were used for imaging. Z-scan was performed at 0.1% power of the 488-nm laser with 100 nm step between the scanning slides.

Fourier-transform infrared spectroscopy (FTIR)

Attenuated total reflection infrared spectroscopy (ATR-FTIR) was performed using a Bruker Vertex 70 spectrometer equipped with a diamond ATR element. The resolution was 4 cm^{-1} and all spectra were processed using Origin Pro software. The spectra were averaged (3 spectra with 256 co-averages), smoothed applying a Savitzky-Golay filter (2nd order, 9 points) and then the second derivative was calculated applying a Savitzky-Golay filter (2nd order, 11 points).

Relative secondary and quaternary organization was evaluated by integrating the area of the different secondary structural contribution in the amide band I, as previously described^{4,5}.

Scanning Electron Microscopy (SEM)

FUS protein condensates were aged and sampled at 30 min, 90 min, 5 h and 24 h at room temperature. The samples were plunge-frozen by immersing into liquid nitrogen-cooled ethane without washing. Samples were then freeze-dried in a liquid nitrogen-

cooled turbo freeze-drier (Quorum K775X). After that, the samples were coated with 15 nm iridium using a Quorum K575X sputter coater. The images were taken by FEI Verios 460 scanning electron microscope run at 1 - 2 keV accelerating voltage. Secondary electron images were acquired using a high-resolution Through-Lens detector in full immersion mode.

Micropipette Aspiration

The sample chamber for micropipette aspiration is a 360 μm -deep chamber comprised of three double-sided sticky spacers (Life Technologies) stacked together and then sandwiched by two pieces of No. 1.5 coverslips (Corning). To insert the micropipette tip to the chamber we cut a 2 mm x 360 μm opening on the side of the silicone spacer. To prevent condensates from wetting the coverslips, the surfaces of coverslips are plasma treated and then PEG-silane coated. To passivate the glass surface, we first clean the coverslip using a plasma cleaner (PDC-32G, Harrick Plasma) at high RF level for 60 seconds. Then we treat the cleaned glass surface with 3-[methoxy(polyethyleneoxy)6-9]propyltrimethoxysilane (SIM6492.7, Gelest) at room temperature for 24 hours. Before use, the cover glass is thoroughly washed with DI water to remove any residual silane. To generate micropipettes, we heat and pull 1 mm glass capillaries (World Precision Instrument) with a micropipette puller (P97, Sutter Instrument) and cut the tapered tip with a microforge (MF830, Narishige) to an inner diameter of 4 - 10 μm . Glass pipettes are plasma treated for one minute at high RF level (PDC-32G plasma cleaner, Harrick Plasma). Then the micropipette tips are passivated with PEG-silane overnight at room temperature following the same method described above for the coverslips. To generate FUS condensates, we dilute a concentrated FUS stock solution with water. The final solution contains 1.5 μM FUS, 2.5 mM Tris, 50 mM KCl, 0.05 mM DTT, 0.25% glycerol, pH 7.4. Micropipette aspiration is conducted on a Leica SP5 confocal microscope equipped with a home-built micromanipulation system. The condensates with diameters ranging from 20 μm – 40 μm are used. During each experiment, a condensate is aspirated into a suction pipette. The negative pressure in the suction pipette is applied via a vacuum controller (Fluigent) with a resolution of 0.75 Pa and a response time of 2 seconds. Several pressure steps are used for the measurement of each condensate. Videos of the

aspirated condensate is recorded as the negative pressure steps between different values. Tongue length values are extracted from the videos using ImageJ. Prior to measuring the viscosity of the FUS condensates, we pre-calibrate the system with a PEG-Dextran aqueous two-phase system using the method in ⁶. Specifically, we use an aqueous solution of 5 wt % PEG 6 kDa (Sigma) and 6.4 wt % Dextran 500 kDa (Spectrum). The solution phase separates under room temperature. We measure the true viscosity of the dextran-rich and the PEG-rich phases using a rheometer (DHR-3, TA Instruments). Taking these viscosity values, we measure an M factor of 76 for our micropipette aspiration system. The M factor is used for calculating the viscosity of FUS condensate samples. The elastic modulus of the sample is calculated using the analysis in⁷

Spatial Dynamic Mapping (SDM)

By collecting time-lapse images, it is possible to analyze the time dependence of the spatial variance, σ^2 , of the difference signal, d , obtained by subtracting the first image from each subsequent one^{8,9}:

$$\sigma^2(\Delta t) = \int |d(x, y; \Delta t)|^2 dx dy$$

where $d(x, y; \Delta t) = I(x, y; \Delta t) - I(x, y; 0)$, in which $I(x, y; \Delta t)$ is the intensity of each frame at time $t = \Delta t$.

We divided each frame into ROIs of about $2 \times 2 \mu\text{m}^2$, and extracted the spatial variance, $\sigma^2(\Delta t)$, from each ROI. We averaged the results of at least 100 frame pairs for each time interval and ROI, plotted the curve and extract the characteristic time from its exponential behavior. Finally, we obtained heat maps for different condensate cross-section. Calibration performed on aqueous suspension of nanoparticles confirmed the direct proportionality of the decay time versus the diffusion coefficient (see next section for more details). By reducing the numerical aperture of the condenser lens, NA_C , the white light can be made partially coherent in a thin volume whose thickness, θ_z , is proportional to the light wavelength, λ , and NA_C via: $\theta_z = \frac{\lambda}{NA_C^2}$ so that for white light illumination and $NA_C \sim 0.15$, $\theta_z \sim 20 \mu\text{m}^{10-12}$. This permitted us to extract information coming only from specific regions, namely the middle and bottom plane.

Spatial Dynamic Mapping (SDM) calibration

We performed a series of tests to calibrate our novel SDM approach. To do that, we used three aqueous solution of polystyrene particles of different sizes, 47, 100 and 200 nm in diameter at a concentration of 0.1 w/v%.. For each sample we collected a series of high speed images (at least 1000 frames at either 220 or 475 fps) and we divided each frame into ROIs and for each we extracted the characteristic decay as discussed in the previous section. We then built heat maps showing for each nanoparticle size the distribution of the decay time. This is supposed to be uniform within the sample although some fluctuation due to local experimental error is present. The results are shown in Fig. S3 where it is possible to appreciate the capability of this new approach to discriminate between different tracers size locally.

Backscattering Confocal Microscopy Speckle Analysis

The FUS condensate is formed using the same method as used for the condensates studied with micropipette aspiration. A 24-hr old condensate is imaged using the reflection mode of a point scanning confocal microscope (Zeiss LSM 980) to collect the backscattered signal. The reflection mode uses a T80/R20 filter in the optical path and collects the same wavelength of light as the excitation wavelength. We use a 40x water-immersion objective with a numerical aperture of 1.1, and set the pinhole size to 1 Airy unit. We use a 405-nm wavelength laser for which the range of scattering vectors that contribute to the speckle pattern is $q = 36.4 \mu\text{m}^{-1}$ to $q = 41.2 \mu\text{m}^{-1}$, where we adjust the wavelength to account for the index of refraction of water. A series of single-plane images at the equatorial plane are collected at 53 ms per frame for 1 min. The intensity correlation is calculated as discussed in¹³. In brief, the intensity correlation function is defined using $c_I(\vec{x}, t, \tau) = \frac{\langle I(\vec{x}, t)I(\vec{x}, t+\tau) \rangle}{\langle I(\vec{x}, t) \rangle \langle I(\vec{x}, t+\tau) \rangle} - 1$, where the brackets mean averaging over nearby pixels. We determine the size of a speckle by calculating the spatial correlation of the image and use a Gaussian window whose width is this size, which is 1.6 pixels, to average the neighboring pixels in calculating the temporal correlations. The intensity correlation is normalized by the image contrast, defined as the correlation at $\tau = 0$, giving $\tilde{c}_I(\vec{x}, t, \tau) = \frac{c_I(\vec{x}, t, \tau)}{c_I(\vec{x}, t, 0)}$. For each pixel at each

lag time, we average the intensity correlation over time to obtain the time-averaged intensity correlation.

We emphasize that, although we are performing a scattering experiment, we are nevertheless imaging the sample with a confocal microscope; therefore, the information provided by this experiment is sensitive to very small motions, which cause the speckle intensity to vary, but is still localized to the diffraction volume.

The correlation function can be approximated by a stretched exponential, $C_\tau(\tau) \sim Ae^{-(\tau/\tau_c)^p} + B$, where A and B are constants, p is the stretching exponent and τ_c is the decay time, as shown by the logarithmic plots of $C_\tau(\tau)$ as a function of τ^p in Fig. 4b in the main text. We use $p = 0.4$, although the best fit varies slightly, between $0.3 \leq p \leq 0.5$, for all the speckles in the image. Similarly, the plateau value varies across the image, with many speckles decaying completely ($B = 0$) while others have plateaus as high as $B = 0.8$.

We validate the scattering result using 0.2% v/v monodispersed suspensions of 120 nm diameter polystyrene beads and confirm that our technique generates the correct correlation functions, from which we can determine the expected diffusion coefficient.

FUS Minimal Coarse-Grained Simulations

We employ a minimal model for FUS proteins recently developed¹⁴, in which we integrate: (1) peptide interaction binding energies of disordered vs. structured Low-Aromatic-Rich Kinked Segments (LARKS) from atomistic simulations¹⁵, and (2) interfacial free energies and protein domain contact probabilities of FUS (full-sequence) condensates evaluated through residue-resolution coarse-grained simulations¹⁶. In our minimal simulations, we model FUS proteins as 20-bead Lennard-Jones (LJ) polymers in which the different domains of FUS (PLD (residues 1–165), RGG1 (residues 166–284), RRM (residues 285–371), RGG2 (residues 372–422), ZF (residues 423–453) and RGG3 (residues 454–526)) are coarse-grained, with one bead representing ca. 26 amino acids. That is, 6 beads for the FUS-PLD, and 14 beads for the RGG1, RRM, RGG2, ZF, and RGG3 domains. A ratio of 6/20 PLD *versus* total FUS beads recapitulates the ratio of PLD *versus* total FUS amino acids (i.e.,

163/526). The solvent is explicitly modelled using single-bead LJ particles that mimic water-water and water-ion interactions.

Beads that are not directly bonded to each other, establish non-bonded interactions described via the LJ potential:

$$V(r) = 4\epsilon \left[\left(\frac{\sigma}{r} \right)^{12} - \left(\frac{\sigma}{r} \right)^6 \right]$$

where ϵ is the depth of the LJ potential, r the distance between two beads, and σ the molecular diameter of each

bead. The mass of every bead was chosen to be $m^* = 1$ (in reduced units). The parameters (ϵ and σ) for the various self- and cross-interactions are shown in Tables S1 and S2. For convenience, we employ reduced units, which are defined as: $T^* = k_B T / \epsilon$, $\rho^* = (N/V)\sigma^3$, $p^* = p\sigma^3/\epsilon$, and time as $t^* = t/(\sigma(m/\epsilon)^{1/2})$.

The cut-off of the LJ interactions is set to 3 times the value of σ . Bonds between consecutive beads are modelled

with a harmonic potential $V_{\text{har}} = K(r - r_0)^2$ of $K = 40 \epsilon/\sigma^2$, and a resting position of $r_0 = 1.3\sigma$. Furthermore, we apply an angular potential of the form, $V_{\text{ang}} = K_{\theta} (\theta - \theta_0)^2$, between consecutive bonds, with an angular constant of $K_{\theta} = 0.2 \epsilon/\text{rad}^2$ and a resting angle of $\theta_0 = 180^\circ$ for fully disordered PLD FUS replicas, and with a constant of $K_{\theta} = 4 \epsilon/\text{rad}^2$ and $\theta_0 = 180^\circ$ for FUS with ordered PLD, to account for the partial rigidification of the proteins after exhibiting the disorder-to-order fibrillar transition¹⁷. The model has been parameterized to recapitulate the observed behaviour in FUS proteins with both disordered-like and structured-like PLD interactions (Figs. 3 and S7 of Ref.¹⁴) and to reproduce the relative density between water and FUS condensates^{18–20}.

To dynamically mimic²¹ the structural diversity of FUS proteins during aging, we employ a time-dependent minimal coarse-grained algorithm^{14,17}. Based on the above minimal coarse-grained parametrization (Tables S1 and S2), we start with a system

composed of a homogeneous single phase of FUS proteins with fully disordered PLDs (Fig. 5B of the main text). Then, FUS-PLD domains can spontaneously transition from their fully disordered state to the ordered state depending on the local environment. Every 100 simulation timesteps, the algorithm evaluates whether the conditions around each fully disordered FUS protein are favorable for undergoing an ‘effective’ disorder-to-order cross- β -fibrillar transition (the exact conditions are described below), and thus modify the protein parameters given in Tables S1 and S2, to those corresponding to ordered PLD-FUS proteins. These conditions are evaluated on the central bead of the PLD, which is a good proxy for the average position of the LARKS found in the PLD of FUS¹⁴.

Our dynamic algorithm changes the identity of two FUS chains from the fully disordered state to the ordered PLD interaction parameters once the two following conditions are met: (1) Their two central beads are at a smaller distance than 2.75σ , and (2) both central beads are surrounded, within a cut-off distance of 2.75σ (a sensible distance close to the maximum distance at which FUS-PLD beads can still attractively interact; the potential cut-off is 3.25σ), by at least four other central beads and six solvent particles (i.e., characteristic crowded environment of a FUS-rich liquid phase described in previously²² through all-atom and residue-resolution simulations). Since it has been recently reported (via PMF atomistic simulations) that strong protein binding between structured FUS LARKS occurs after undergoing a disorder-to-cross- β -sheet transition (typically of the order of 20 to 45 $k_B T$; see Ref.¹⁴), we set the transition towards ordered-PLD FUS replicas to be irreversible. To carry out these simulations, we employ the USER-REACTION²³ package of LAMMPS²⁴ which allows us to change the topology of the underlying system components on-the-fly.

The criterion that at least four peptides should be in close contact to trigger a disorder-to-order transition has been chosen based on the following arguments. Four interacting peptides is the minimal system where all the different types of stacking and hydrogen bonding interactions that stabilize the β -sheet fibrillar ladder are fulfilled; i.e., two interacting steps of the ladder each made of a pair of β -sheet peptides. Thus, considering fewer interacting peptides (e.g., only three or two) would severely underestimate the required interaction strength among ordered LARKS to form

irreversible inter-peptide β -sheet motifs, and subsequently, erroneously preclude the formation of kinetically arrested states at the coarse-grained level. Atomistic simulations from Refs.^{14,17,25} show that the strength of interactions among four ordered peptides is already high enough for the peptides to remain stably bound upon thermal fluctuations. Hence, if we made the criterion even more stringent (i.e., by requiring clustering of five or more peptides), the strength of interactions among the system would remain consistent with kinetic arrest at the coarse-grained level. However, a stringent criterion would now render the coarse-grained simulations prohibitively expensive. That is, much longer simulation timescales would be needed to capture the rarer higher-density fluctuations that could result in the spontaneous formation of clusters of five or more peptides (as opposed to the more frequent fluctuations that yield clusters of four peptides; as shown in Fig. 5c of the main text).

The system size of our FUS minimal simulations (Fig. 5 of the main text) contained 12300 solvent particles and 1088 protein replicas. NVT simulations were run at $T^* = 3.5$ and at density of $\rho^* = 0.25$. Temperature was kept constant with a Nosé–Hoover thermostat²⁶ and with a relaxation time of $\tau^* = 0.4$. The Verlet equations of motion are integrated with a timestep of $\tau^* = 0.0004$. We employ the Direct Coexistence method as described in Refs.^{18,27,28} and the LAMMPS Molecular Dynamics software²⁴.

Table S1: Model parameters for the different ϵ values in reduced units.

	Solvent	PLD ordered	PLD disordered	Non-PLD ordered	Non-PLD disordered
Solvent	3.50	2.20	1.07	1.15	1.15
PLD ordered	2.20	3.80	1.20	1.50	1.20
PLD disordered	1.07	1.20	1.45	1.25	1.25
Non-PLD ordered	1.15	1.50	1.25	1.50	1.25
Non-PLD disordered	1.15	1.20	1.25	1.25	1.25

Table S2: Model parameters for the different σ values in reduced units.

	Solvent	PLD ordered	PLD disordered	Non-PLD ordered	Non-PLD disordered
Solvent	1.00	1.15	1.15	1.15	1.15
PLD ordered	1.15	1.30	1.30	1.30	1.30
PLD disordered	1.15	1.30	1.30	1.30	1.30
Non-PLD ordered	1.15	1.30	1.30	1.30	1.30
Non-PLD disordered	1.15	1.30	1.30	1.30	1.30

References

1. Murakami, T. *et al.* ALS/FTD Mutation-Induced Phase Transition of FUS Liquid Droplets and Reversible Hydrogels into Irreversible Hydrogels Impairs RNP Granule Function. *Neuron* **88**, 678–690 (2015).
2. Qamar, S. *et al.* FUS Phase Separation Is Modulated by a Molecular Chaperone and Methylation of Arginine Cation- π Interactions. *Cell* **173**, 720-734.e15 (2018).
3. Shen, Y. *et al.* Biomolecular condensates undergo a generic shear-mediated liquid-to-solid transition. *Nat Nanotechnol* **15**, 841–847 (2020).
4. Ruggeri, F. S. *et al.* Infrared nanospectroscopy characterization of oligomeric and fibrillar aggregates during amyloid formation. *Nat Commun* **6**, 1–9 (2015).
5. Ruggeri, F. S., Mannini, B., Schmid, R., Vendruscolo, M. & Knowles, T. P. J. Single molecule secondary structure determination of proteins through infrared absorption nanospectroscopy. *Nat Commun* **11**, 2945 (2020).
6. Wang, H., Kelley, F. M., Milovanovic, D., Schuster, B. S. & Shi, Z. Surface tension and viscosity of protein condensates quantified by micropipette aspiration. *Biophysical Reports* **1**, 100011 (2021).
7. Theret, D. P., Levesque, M. J., Sato, M., Nerem, R. M. & Wheeler, L. T. The Application of a Homogeneous Half-Space Model in the Analysis of Endothelial Cell Micropipette Measurements. *J Biomech Eng* **110**, 190–199 (1988).
8. Linsenmeier, M. *et al.* Dynamic arrest and aging of biomolecular condensates are modulated by low-complexity domains, RNA and biochemical activity. *Nat Commun* **13**, 3030 (2022).
9. Cerbino, R. & Trappe, V. Differential Dynamic Microscopy: Probing Wave Vector Dependent Dynamics with a Microscope. *Phys Rev Lett* **100**, 188102 (2008).

10. Riccomi, M., Alberini, F., Brunazzi, E. & Vigolo, D. Ghost Particle Velocimetry as an alternative to μ PIV for micro/milli-fluidic devices. *Chemical Engineering Research and Design* **133**, 183–194 (2018).
11. Pirbodaghi, T., Vigolo, D., Akbari, S. & DeMello, A. Investigating the fluid dynamics of rapid processes within microfluidic devices using bright-field microscopy. *Lab Chip* **15**, 2140–2144 (2015).
12. Buzzaccaro, S., Secchi, E. & Piazza, R. Ghost Particle Velocimetry: Accurate 3D Flow Visualization Using Standard Lab Equipment. *Phys Rev Lett* **111**, 048101 (2013).
13. Aime, S., Sabato, M., Xiao, L. & Weitz, D. A. Dynamic Speckle Holography. *Phys Rev Lett* **127**, 088003 (2021).
14. Garaizar, A. *et al.* Aging can transform single-component protein condensates into multiphase architectures. *Proceedings of the National Academy of Sciences* **119**, (2022).
15. Robustelli, P., Piana, S. & Shaw, D. E. Developing a molecular dynamics force field for both folded and disordered protein states. *Proc Natl Acad Sci U S A* **115**, E4758–E4766 (2018).
16. Joseph, J. A. *et al.* Physics-driven coarse-grained model for biomolecular phase separation with near-quantitative accuracy. *Nature Computational Science* **2021 1:11 1**, 732–743 (2021).
17. Tejedor, A. R. *et al.* Ageing critically transforms the network connectivity and viscoelasticity of RNA-binding protein condensates but RNA can prevent it. *bioRxiv* (2022) doi:10.1101/2022.03.30.486367.
18. Espinosa, J. R., Garaizar, A., Vega, C., Frenkel, D. & Collepardo-Guevara, R. Breakdown of the law of rectilinear diameter and related surprises in the liquid-vapor coexistence in systems of patchy particles. *J Chem Phys* **150**, 224510 (2019).
19. Krainer, G. *et al.* Reentrant liquid condensate phase of proteins is stabilized by hydrophobic and non-ionic interactions. *Nat Commun* **12**, 1085 (2021).
20. Bock, A. S. *et al.* N-terminal acetylation modestly enhances phase separation and reduces aggregation of the low-complexity domain of RNA-binding protein fused in sarcoma. *Protein Sci* **30**, 1337–1349 (2021).
21. Mountain, G. A. & Keating, C. D. Formation of Multiphase Complex Coacervates and Partitioning of Biomolecules within them. *Biomacromolecules* **21**, 630–640 (2020).
22. Welsh, T. J. *et al.* Surface Electrostatics Govern the Emulsion Stability of Biomolecular Condensates. *Nano Lett* **22**, 612–621 (2022).
23. Gissinger, J. R., Jensen, B. D. & Wise, K. E. Chemical Reactions in Classical Molecular Dynamics. *Polymer (Guildf)* **128**, 211–217 (2017).
24. Plimpton, S. Fast Parallel Algorithms for Short-Range Molecular Dynamics. *J Comput Phys* **117**, 1–19 (1995).
25. Garaizar, A., Espinosa, J. R., Joseph, J. A. & Collepardo-Guevara, R. Kinetic interplay between droplet maturation and coalescence modulates shape of aged protein condensates. *Scientific Reports* **2022 12:1 12**, 1–13 (2022).
26. Nosé, S. A unified formulation of the constant temperature molecular dynamics methods. *J Chem Phys* **81**, 511 (1998).
27. Ladd, A. J. C. & Woodcock, L. v. Triple-point coexistence properties of the lennard-jones system. *Chem Phys Lett* **51**, 155–159 (1977).

28. García Fernández, R., Abascal, J. L. F. & Vega, C. The melting point of ice Ih for common water models calculated from direct coexistence of the solid-liquid interface. *J Chem Phys* **124**, 144506 (2006).

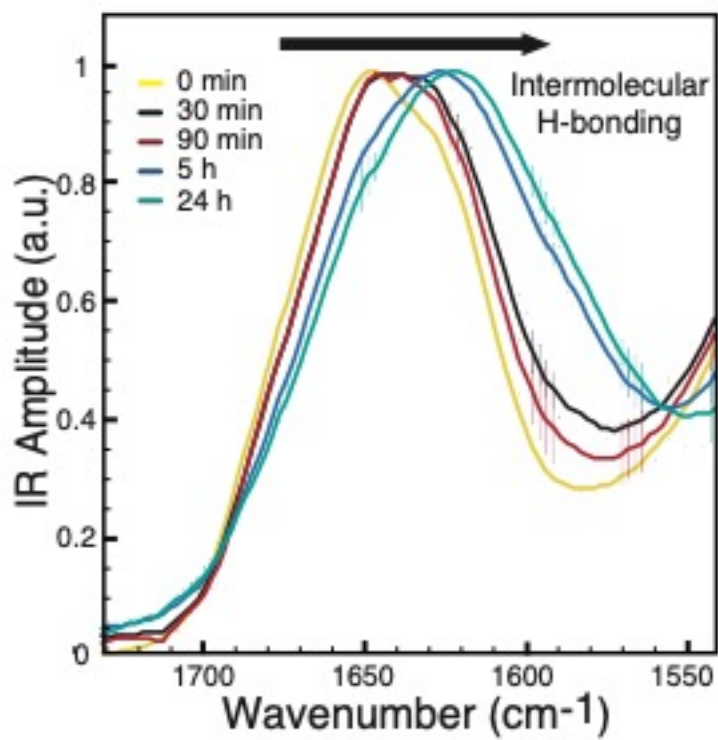


Fig. S1, The shift of the wavenumber in IR spectra of the FUS condensates incubated for different time at room temperature.

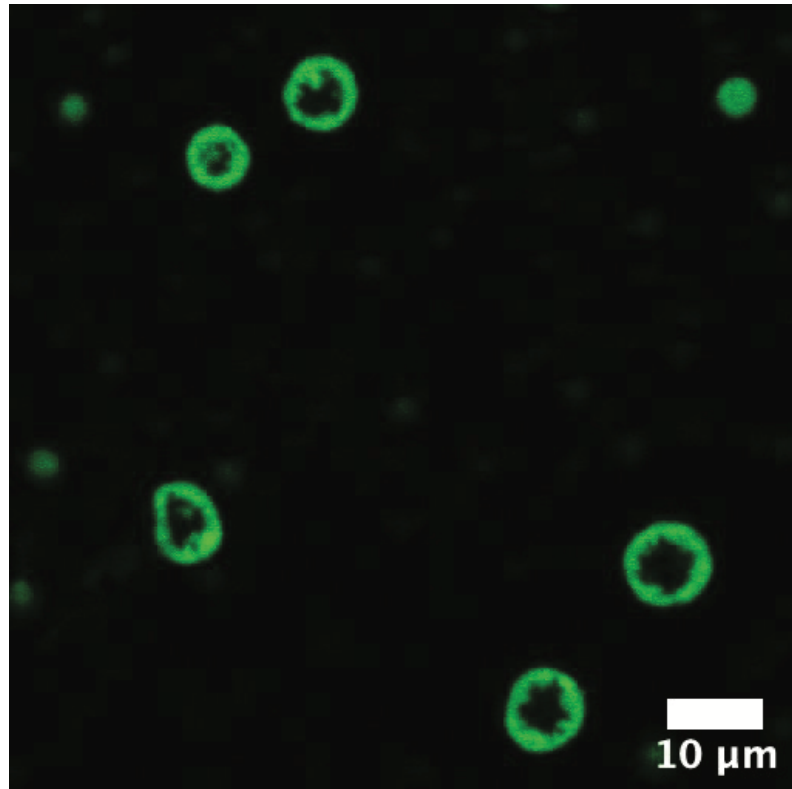


Fig. S2, 48h-incubated condensates demonstrate core-shell structure after dissolution by mixing with 1M KCl.

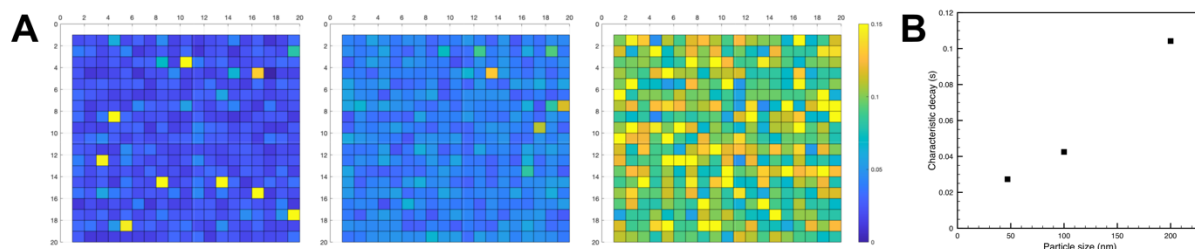


Fig. S3, Nanoparticle calibration of the system. A – Spatial Dynamic Mapping (SDM) for 47, 100 and 200 nm particle respectively showing a uniform distribution of the characteristic decay time (values in seconds). B – Average characteristic decay time obtained from SDM versus particle size. The error bar (standard error) is smaller than the symbol.

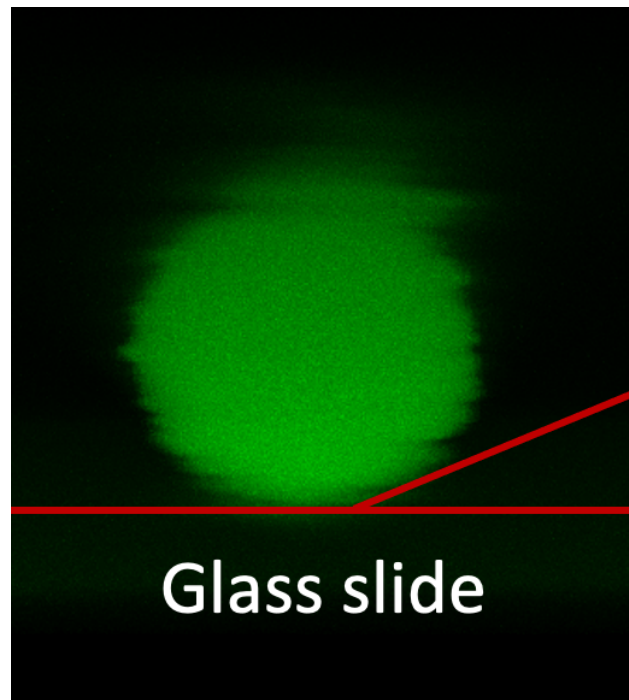


Fig. S4, Confocal 3D scanning reconstruction in the z-direction of a FUS condensate in contact with a plasma-treated glass slide. Each glass slide in this work has been exposed to plasma treatment for 300 s to render it hydrophilic and maximize the contact angle, estimated to be about 160° . The condensate in the image is about $10\ \mu\text{m}$ in diameter.

Mov. S1, Confocal Z-scan of a 24h-incubated FUS protein condensate.